nature catalysis

REVIEW ARTICLE

https://doi.org/10.1038/s41929-018-0181-7

Characteristics and performance of two-dimensional materials for electrocatalysis

Xinyi Chia[1] and Martin Pumera[2*]

The unique anisotropy and electronic properties of 2D materials have sparked immense interest in their fundamental electrochemistry and wide spectrum of applications. Beginning with the prototype 2D material — graphene — studies into an extensive library of other ultrathin layered structures have gradually emerged. Among these are the transition metal dichalcogenides, layered double hydroxides, metal carbides and nitrides (MXenes) and the black phosphorus family of monoelemental compounds. In this Review, we discuss the similarities of these 2D materials and highlight differences in their electrochemical and electrocatalytic properties. Recent progress on 2D materials for energy-related electrocatalysis in industrially important reactions is presented. Together this shows that dimensionality and surface characteristics are both vital aspects to consider when designing and fabricating compounds to achieve desired properties in specific applications.

Two-dimensional (2D) nanomaterials were introduced with graphene: an atomically thin carbon material obtained from the delamination of graphite that possesses remarkable anisotropic physical and electronic properties[1]. Following graphene's precedent, other classes of ultrathin 2D nanomaterials were explored, including single- or few-layered transition metal dichalcogenides (TMDs), metal oxides, layered double hydroxides (LDHs), hexagonal boron nitride (h-BN), graphitic carbon nitride (g-C_3N_4), metal carbides and nitrides (collectively known as MXenes) and a family of monoelemental compounds: black phosphorus (or phosphorene), arsenene, antimonene and bismuthine[2–8]. These materials have thicknesses of one or several atoms and a hallmark feature is the way they layer with unique bonding interactions. Strong covalent bonds extend through the atoms within the plane whereas weak van der Waals interactions exist between layers. Weak interlayer bonding allows convenient exfoliation of these materials into thinner nanosheets comprising of a few layers, or a monolayer. These ultrathin sheets typically demonstrate properties that are dissimilar to the parent bulk material due to anisotropy.

The early application of 2D nanomaterials as lubricants was a result of their layered nature. Over the years, 2D nanomaterials have diversified into many applications dictated by their electronic structures and intrinsic physical properties. Graphene is a zero band gap semimetal where electrons are highly mobile and exhibit exceptional conductivity[2,3]. Equipped with a varying band gap, other 2D nanomaterials, such as TMDs, LDHs, metal oxides and MXenes present versatile opportunities. By tweaking the transition metal or chalcogen type, TMDs can achieve a spectrum of properties[5] encompassing insulators (HfS_2), semiconductors (MoS_2), semimetals ($PtSe_2$) and true metals (NbS_2). Insulating h-BN and semiconducting g-C_3N_4 are prized for their thermal and chemical stability[3,9]. Thanks to their vast array of properties, 2D nanomaterials hold promise in the fields of electronics, sensors and catalysis. As developments in sustainable energy garner global attention, it has become imperative to evaluate the efficacy of various 2D nanomaterials in these areas. Electrocatalysis lies at the heart of clean energy conversion in future technologies via the hydrogen evolution reaction (HER), hydrogen oxidation reaction (HOR), oxygen reduction reaction (ORR), oxygen evolution reaction (OER) and carbon dioxide reduction reaction (CO_2RR). 2D nanomaterials are pursued as economical alternatives to expensive platinum-based catalysts for such reactions.

The allure of 2D materials in catalysis can be mapped to three aspects: specific surface area, mechanical properties and conductivity (thermal and electric)[2]. 2D materials have maximal surface to bulk ratios, providing a high density of surface active sites, which favours surface-active applications. Excellent mechanical properties confer catalyst durability and thermal conductivity facilitates the diffusion of heat produced during exothermic reactions. Additionally, the tunable electronic properties of 2D materials tailor catalytic performance. Robust mechanical structures, wide surface area and high density of active sites in 2D nanomaterials are advantageous compared with bulk materials for catalyst stability and activity. Compared to bulk materials, 2D materials are also preferred building blocks for constructing hierarchical composite catalysts.

The overarching aim of this Review is to compare the electrocatalytic and electrochemical properties across 2D nanomaterials. First, we describe their distinct structures. Secondly, we discuss the inherent electrochemistry of the materials arising from their intrinsic activity or redox reactions, which affects their stability in a stipulated potential window. Thirdly, we highlight the implications of anisotropy and impurities on the electron transfer at 2D materials. Strategic applications in electrocatalysis of the different families of 2D nanomaterials are also analyzed, focusing on the role of edges and surface characteristics. In closing, we present future perspectives for the field of 2D nanomaterials.

Structure of 2D materials

The distinct structural coordination of the 2D materials are illustrated in Fig. 1. Graphene is a single layer of graphite consisting of a honeycomb-like structure of sp^2 hybridized carbon atoms. Yet current techniques to fabricate mono- or few-layer graphene sheets result in graphene derivatives with defects and oxygen-containing

[1]Division of Chemistry and Biological Chemistry, School of Physical and Mathematical Sciences, Nanyang Technological University, Singapore, Singapore. [2]Centre for Advanced Functional Nanorobots, Department of Inorganic Chemistry, Faculty of Chemical Technology, University of Chemistry and Technology, Prague, Czech Republic. *e-mail: martin.pumera@vscht.cz

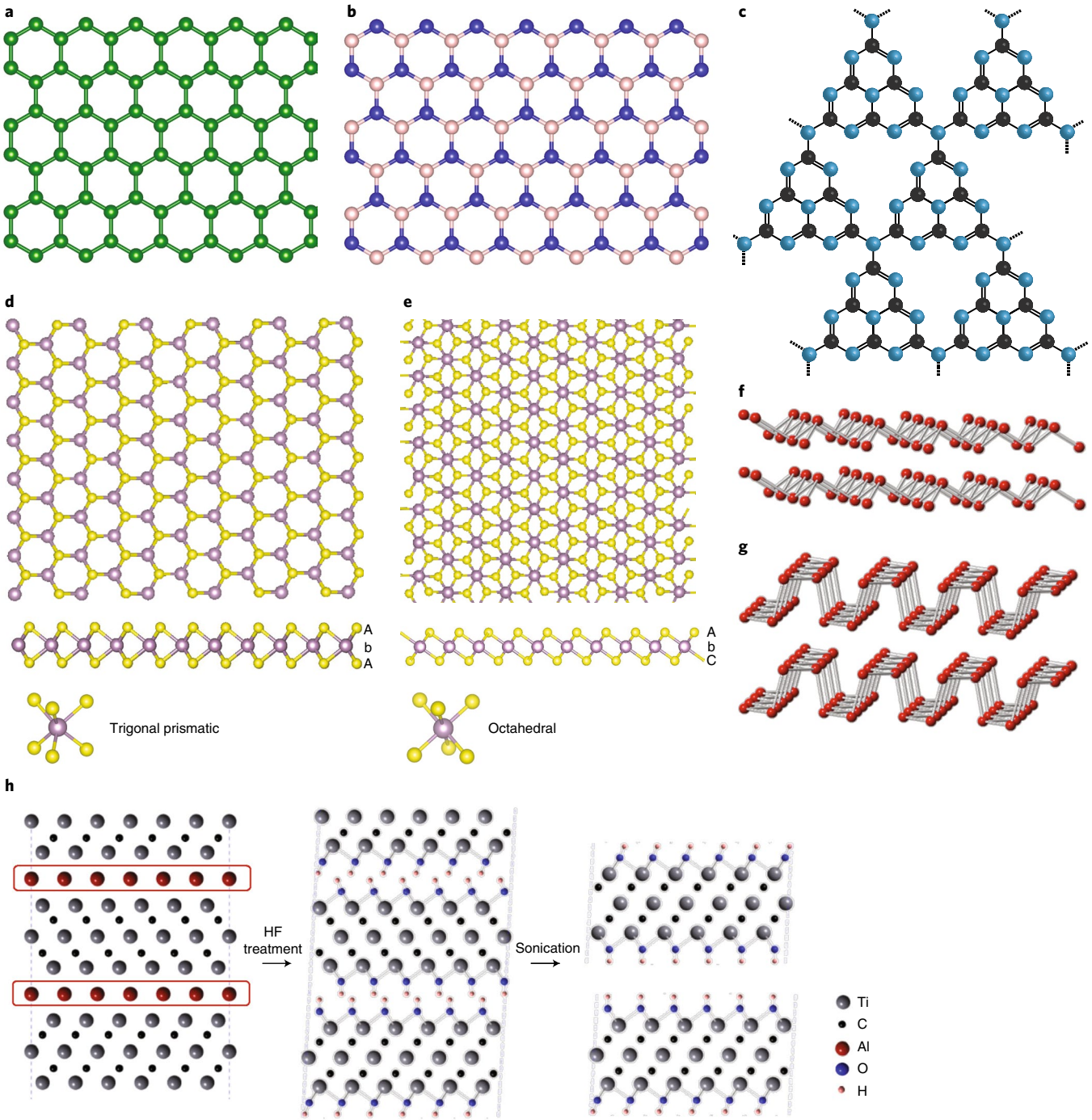

Fig. 1 | Schematic structural configurations of 2D materials. a, Graphene. **b**, h-BN. **c**, Heptazine-based g-C_3H_4. **d**,**e**, TMDs as exemplified by MoS_2 in 2H-phase (**d**) and 1T-phase (**e**). **f**,**g**, Black phosphorus and pnictogens in rhombohedral (**f**) and orthorhombic (**g**) phases. **h**, MXenes as exemplified by the exfoliation of Ti_3AlC_2. Credit: Figure reproduced from ref. [8], American Chemical Society (**a**,**b**), ref. [17], RSC (**c**); ref. [5], SNL (**d**,**e**); ref. [7], Wiley (**f**,**g**); and ref. [18], Wiley (**h**)

impurities that engender properties deviant from pristine graphene[10]. Such graphene derivatives are known as chemically modified graphene.

As binary analogues to graphene, TMDs are represented in MX_2 stoichiometry where M is a transition metal belonging to groups IVB–VIIIB and X is a chalcogen from group VIA (S, Se, Te). Contingent on the *d* electron count, the chalcogen atoms occupy either the trigonal prismatic or octahedral sites around the central transition metal in a TMD. Contrary to graphene, TMDs exhibit polymorphism: trigonal (1T), hexagonal (2H) and rhombohedral (3R) forms. For example, when in their bulk state, group VIB TMDs such as MoS_2 exist in the 2H-phase, which is thermodynamically favoured, whereas exfoliation to monolayers by Li-intercalation induces a phase transformation to the 1T-phase[11,12]. 1T-phase TMDs have been stabilized by covalent functionalization and transition metal doping[13–15].

Layered oxides comprise metal hydroxides ($M(OH)_2$) or metal oxyhydroxides (MOOH) possessing octahedral MO_6 units in a

stacked conformation with a proton or water molecule interleaved between layers. They may also be classified as LDHs when they consist of divalent and trivalent cations manifesting in positively brucite-like layers and balanced by negatively charged anions along with structural water within the interlayer[16].

The structural lattice in boron nitride resembles the carbon arrangement in graphene except that an equal number of boron and nitrogen atoms are present. In a honeycomb structure, h-BN sheets comprise B and N atoms in a sp^2 configuration. Likewise, carbon nitride materials are constructed from carbon- and nitrogen-containing heterocycles with heptazine or triazine rings connected in sp^2-bonded N atoms such as –NH–, =NH and $–NH_2$ functional groups[17].

One of the newest additions to the 2D nanomaterials domain is the family of MXenes commencing with the discovery of Ti_3C_2 in 2011[18]. The general formula of an MXene is $M_{n+1}X_nT_x$ (n = 1–3) where M is a transition metal belonging to the earlier groups, X is carbon or nitrogen and may be terminated by functional groups indicated as T_x such as oxygen, fluorine or hydroxyl functional moieties[19]. MXenes undertake three different stoichiometries in a close-packed octahedral geometry: M_2X, M_3X_2 and M_4X_3. Referred to as MAX phase, the parent compound of MXene is composed of $M_{n+1}X_n$ layers that are interleaved with an A element from groups IIIA or IVA. Due to the metallic M–A bonds, MXenes are obtained by selective etching of A (ref. [19]). In contrast to graphite and bulk TMDs, the interlayer interactions in a stacked assembly of MXene sheets are at least twice as strong[20]. Therefore, mechanical exfoliation of MXenes to individual layers is inefficient and intercalation methods are required to achieve complete delamination to graphene-like thinness[8,21].

Monoelementals of group VA (pnictogens) such as black phosphorus, arsenic, antimony and bismuth are commonly referred as phosphorene, arsenene, antimonene and bismuthene. Thermodynamically stable black phosphorus is in the orthorhombic phase, where six-member rings of atoms exist in chair conformation, whereas the rhombohedral structure exists under high-pressure. Heavy pnictogens, like As, Sb and Bi, manifest in a rhombohedral structure[6]. Despite having similar stacking as multilayer graphene sheets, these pnictogens, except black phosphorus, exhibit stronger interlayer interactions than the materials bound with van der Waals forces[7].

Electrochemical stability of 2D materials as electrodes

Despite the proliferation of research into electrochemical applications for 2D nanomaterials, the irony is that current understanding of their electrode stability is inadequate. Such knowledge is indispensable because the materials may experience chemical or structural alterations during operational use. Inadvertently, their efficiency in electrochemical devices may be affected. Electrode stability is explained in terms of their inherent electrochemistry and inclination towards catalytic reactions depending on the choice of electrolyte and applied potential window. In electrocatalysis, inherent electrochemistry describes the innate redox behaviour of the electrode material when an electrochemical potential is applied[4]. The electrochemical potentials in this section are reported versus Ag/AgCl electrode.

While pristine graphene shows no inherent electrochemistry over a stable and large window, chemically modified graphenes, which possess extensive carbon–oxygen bonds, manifest multifarious electrochemical reductions originating from their electroactive oxygen functionalities. Oxygen functionalities, such as the peroxyl and aldehyde groups, are reduced at mild conditions whereas carboxyl groups become reduced only at extreme negative potentials ~2.0 V (ref. [22]). Reduction of the oxygen functional groups of graphene oxide is chemically irreversible. During the initial sweep, the intense cathodic wave begins at –0.7 V and peaks over a range from –0.9 V to –1.5 V (ref. [23]). As the cathodic peaks vanish in subsequent scans, there is complete reduction of all electroreducible groups within the first scan.

Binary elemental constituents (the transition metal and the chalcogen) and the formation of inevitable surface oxides govern the inherent electrochemistry of TMDs, which is more multifaceted than graphene materials. Bonde et al. first reported the inherent anodic signals of MoS_2 and WS_2 performed in acidic conditions[24]. X-ray photoelectron spectroscopy (XPS) studies disclose MoS_2 oxidized to yield MoO_3, SO_4^{2-} and S_2^{2-} species and similar observations were also noted for WS_2. Recently, a series of electrochemical studies under neutral conditions demonstrated that bulk and exfoliated group VIB TMDs exhibit oxidative waves ranging from 1.0 V to 1.2 V that arise from the oxidation of the metal centre from +4 to +6, as confirmed by comparisons to the inherent electrochemistry of the associated transition metal oxides[25–27]. Dissimilar to the diselenides or disulfides, bulk and exfoliated $MoTe_2$ and WTe_2 share a distinct anodic wave at 0.5 V that is traced to tellurium electrochemistry resulting in the oxidation to TeO_2 (ref. [28]). The propensity of the TMD towards oxidation also contributes to the inherent electrochemistry. The oxidation peak potential of the group VIB TMDs unveils an increasing trend such that WSe_2 <$MoSe_2$ <WS_2 < MoS_2 (refs [25,26]). These findings coincide with previous studies that tungsten dichalcogenides oxidize more readily than molybdenum dichalcogenides and the diselenides over the disulfides[29]. Moreover, ditellurides are known to be most prone to oxidation[29,30]. In liquid-phase exfoliated TMDs, Coleman and co-workers noted the absence of oxide impurities except for $MoTe_2$ and WTe_2 (ref. [31]). Raman spectra indicated the presence of TeO_2 in the ditellurides where WTe_2 contained a larger amount of oxides. Chalcogen-dependence of the inherent electro-oxidative waves is also witnessed in vanadium and platinum dichalcogenides, where the intrinsic oxidation potentials decrease as one progresses down the chalcogen group[32,33]. Under acidic conditions for HER, the oxidation tendency of TMDs would not be a key consideration as the onset of hydrogen evolution occurs in the negative potential region.

In the pnictogen family, multi-layered phosphorene was the first to be investigated for its electrochemistry and found to possess a lone inherent anodic signal. The anodic signal stems from the oxidation of P(0) to P(V) state to result in P_2O_5 or H_3PO_4 species[34]. Exposure to ambient light, moisture and air readily oxidizes the surface to P_xO_y, which reacts further to H_3PO_4. Due to quantum confinement effects, Martel and co-workers discovered that such degradation of black phosphorus is thickness dependent whereby the extent of passivation increases as the number of layers decreases[35]. Other than the proclivity to oxidation, multi-layered phosphorene also displays a prominent oxygen reduction signal at –0.5 V (ref. [34]). Later, an electrochemical study was extended into layered arsenene, antimonene and bismuthene. Voltammograms of the bulk pnictogens are devoid of electrochemical signals[36]. Upon shear exfoliation, native redox signals of the layered pnictogens materialize. Down the group, the anodic peak potentials of the exfoliated pnictogens become increasingly negative from –0.10 V for arsenene to –0.19 V for bismuthene.

In stark contrast to other 2D nanomaterials, g-C_3N_4 showcases negligible inherent electroactivity[37,38]. Despite the presence of nitrogen atoms, the cyclic voltammograms of g-C_3N_4 synthesized from different methods are featureless[38]. Therefore, no electroactive surface functional groups exist on as-synthesized g-C_3N_4. Akin to pristine graphene, g-C_3N_4 possesses a broad operational window that eliminates inherent interference in electrochemical applications.

The innate electrochemistry of the prototype MXene $Ti_3C_2T_x$ has been examined recently. In an electrolyte of pH 7.0, $Ti_3C_2T_x$ exhibits an intense irreversible oxidation signal at 430 mV that is absent in successive sweeps[39]. This signal is beneficial towards the electrochemical oxidation of nicotinamide adenine dinucleotide (NADH)[39]. Electrochemically oxidized $Ti_3C_2T_x$ that cannot be re-

reduced presents a stable window of operation in electrochemical applications.

Electron transfer at 2D materials

After elucidating the inherent electrochemistry of the 2D nanomaterials, where these electrode materials undergo intrinsic oxidation or reduction, we shift our attention towards their electrode kinetics. The electrode kinetics fundamentally connotes the heterogeneous electron transfer (HET) between the electroactive molecular probes in solution and the solid-state electrode material. Anisotropic, electronic and surface characteristics have been found to exhibit important implications on the electron transfer kinetics.

The anisotropy of graphene materials is manifested in the observed HET rates occurring on the edge and basal planes. On the edge planes of graphite-based highly pyrolytic graphite electrodes, the HET rates of the $[Fe(CN)_6]^{3-/4-}$ redox couple are fast[40]. Conversely, the HET rates are significantly slower on the basal planes[40]. The same trend pans out for a single graphene layer whereby the HET rates of molecular probes like $[Fe(CN)_6]^{3-/4-}$, ascorbic acid and NADH are more rapid on the edge than the basal plane[41]. Additionally, defects in graphene materials generate faster HET rates due to a higher electronic density of states (DOS). The energy level of the defect states lies between conduction and valence bands in a disordered pristine sp^2 structure. This fills the DOS within close proximity to the Fermi level[42]. On the contrary, the small overlap of valence and conduction bands of pristine graphene results in a low DOS at the Fermi level. HET rates at defect sites of chemical-vapour-deposited graphene, which had mechanically and chemically induced defects, were an order of magnitude larger compared to that of the basal plane[43].

The oxygen-containing functional groups on graphene strongly influence HET rates towards specific electroactive probes. In a study involving graphene oxide and reduced graphene materials, it bears out that the HET rate increases as the carbon-to-oxygen ratio increases[10]. Reduced graphene oxide, where the oxygen groups have been eliminated, showcases an elevated HET rate and lower charge transfer resistance (R_{ct}) in the $[Fe(CN)_6]^{3-/4-}$ redox probe with respect to graphene oxide[44]. Electrostatic repulsion between the oxygen-containing groups in graphene oxide and the negatively charged $[Fe(CN)_6]^{3-/4-}$ redox probe hinders electron transfer across the electrode–electrolyte interface, leading to slower HET rates in graphene oxide. Specific to surface-sensitive redox probes, like $[Fe(CN)_6]^{3-/4-}$, the effects of oxygen-containing moieties on HET rates do not affect surface-insensitive probes like $[Ru(NH_3)_6]^{3+/2+}$ (ref. [45]).

Being anisotropic, TMDs resemble graphene such that discernible electron transfer properties arise from the edge and basal planes. Gerischer et al. investigated the mechanism of electron transfer at these two orthogonal planes of MoS_2 using $[Fe(CN)_6]^{3-/4-}$, $Fe^{3+/2+}$ and $Cu^{2+/+}$ redox probes and established a correlation to the electronic structure of MoS_2 (ref. [46]). As one might anticipate, the HET rate of the MoS_2 edge plane surpasses that of the basal surface, as also seen in the case of graphene. This phenomenon is attributed to the substantial overlap of the d_{xy} and $d_{x^2-y^2}$ orbitals of the Mo conduction band and orbitals of redox probes. Concurring with this, we ascertained that the edge plane of macroscopic MoS_2 crystals (Fig. 2) demonstrates a fast HET rate where we computed $k^0_{obs} = 4.96 \times 10^{-5}$ cm s^{-1} for $[Fe(CN)_6]^{3-/4-}$ and 1.1×10^{-3} cm s^{-1} for $[Ru(NH_3)_6]^{3+/2+}$ redox probes[47]. By contrast, the pristine basal plane showed sluggish HET rates, approximating zero for both redox probes. Exfoliation of the bulk TMD may either augment or worsen the HET rates towards $[Fe(CN)_6]^{3-/4-}$. Compared to the respective bulk counterparts, faster HET rates were observed for exfoliated $MoSe_2$ and WS_2 across conventional organolithium reagents and aromatic intercalants, yet exfoliated MoS_2 and WSe_2 showed mixed responses: faster in some cases and slower in others depending on the intercalant[26,27]. Sometimes, exfoliation

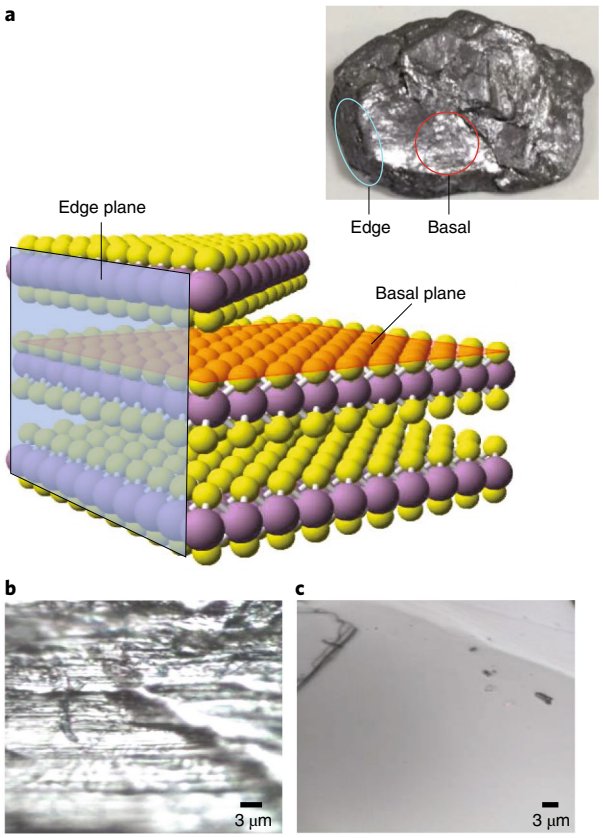

Fig. 2 | Anisotropic effects that influence electron transfer at 2D materials. a, Schematic illustration of edge and basal planes of MoS_2. Inset: macroscopic molybdenite crystal (approx. 190 mm × 280 mm). **b**,**c**, Surface morphologies of edge (**b**) and basal (**c**) planes of MoS_2 by optical microscopy. Credit: Figure reproduced from ref. [47], Wiley

may introduce oxides that impede the electron transfer at the electrode–electrolyte interface.

Electrochemical treatment elicits structural and electronic modifications to the material and is a means to tailor the HET rates of TMDs. Zhang and co-workers prepared exfoliated MoS_2 nanosheets from molybdenite crystal by electrochemical Li-intercalation. An electroreduction of the exfoliated MoS_2 nanosheets conferred improved conductivity to the material leading to faster HET rates for redox probes than before treatment[48]. Our study on bulk and exfoliated MoS_2 also showed higher HET rates towards $[Fe(CN)_6]^{3-/4-}$ upon a preliminary reductive treatment[49]. Yet a preliminary oxidation deteriorated the HET rates of both bulk and exfoliated MoS_2. Density functional theory (DFT) calculations justify electron doping during electroreduction to be the primary factor stabilizing the 1T phase, which improves the electron transfer and catalytic properties for hydrogen evolution. This study was extended to explore the effect of electrotreatment on the HET abilities of other groups of layered TMDs[25,33,50]. It has become a common feature across TMDs that electroreduction of TMDs speeds up HET rates towards $[Fe(CN)_6]^{3-/4-}$ whereas an electro-oxidation may encumber the electron transfer (Fig. 3).

Dopants and impurities are known to alter their electron transfer properties. N-doped graphene, with the electron-donating nitrogen dopants implanted by thermal exfoliation of graphite oxide in an ammonia-saturated environment, showcases accelerated HET rates towards the $[Fe(CN)_6]^{3-/4-}$ redox couple than the undoped graphene[51]. In another case, N-doped graphene prepared through nitrogen plasma treatment of graphene demonstrates higher

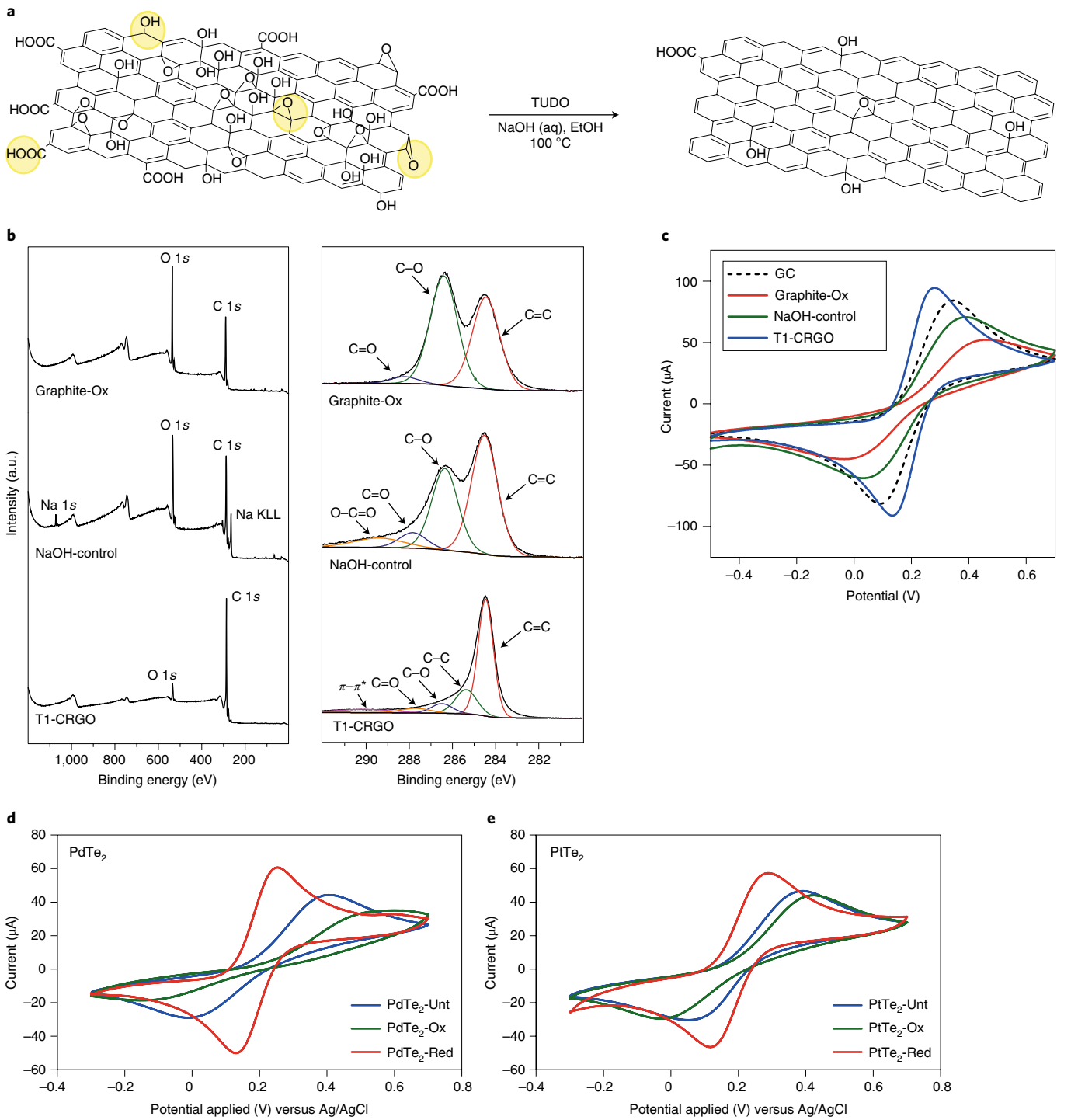

Fig. 3 | Surface characteristics that influence electron transfer at 2D materials. a–c, Schematic illustration of the reduction of functional groups on graphene oxide by thiourea dioxide (TUDO, **a**), XPS spectra of graphite oxide after reduction with NaOH in the absence of TUDO for 2 h at 90 °C (NaOH-control), and after reduction with NaOH and TUDO for 1 h at 90 °C (chemically reduced graphene oxide, T1-CRGO) (**b**), and their cyclic voltammograms recorded in $[Fe(CN)_6]^{3-/4-}$ probes (**c**). **d**,**e**, Voltammograms depicting the changes in electron transfer of the treated $PdTe_2$ (**d**) and $PtTe_2$ (**e**) towards $[Fe(CN)_6]^{3-/4}$ probes. Credit: Figure reproduced from ref. [44], RSC (**a–c**) and ref. [50], American Chemical Society (**d**,**e**)

catalytic activity in the reduction of H_2O_2 than before treatment[52]. Numerous reports also suggest that metal-based contaminants — including Ni, Fe and Co in parts per billion concentrations — in graphene materials account for the enhanced electrocatalytic activity for analytes such as hydrazine and NaHS (refs [53,54]). Similarly, the presence of transition metal dopants in TMDs impacts their eventual HET behaviour towards a $[Fe(CN)_6]^{3-/4-}$ redox probe. Nb- and Ta-doped MoS_2 exhibited marginally slower HET than the undoped MoS_2 whereas a faster HET occurs upon the doping WS_2 with Nb or Ta (ref. [55]).

The anisotropic properties of black phosphorus also contribute to the different electron transfer rates on the edge and basal planes. For

both $[Fe(CN)_6]^{3-/4-}$ and $[Ru(NH_3)_6]^{3+/2+}$ redox probes, faster electron transfer was observed for the edge whereas the slow electron transfer rates on the basal plane manifests into poorly defined redox signals for the basal plane[56]. Likewise, the edge plane of the black phosphorus is more sensitive to the oxidation of ascorbic acid analyte as evident in the larger current as opposed to the mild current of the basal plane[56]. Other members of the pnictogen family reveal that shear exfoliation improves their electron transfer rates. There is a marked increase in HET rate upon shear exfoliation of the bulk pnictogens wherein the most accentuated increase is observed in bismuthene compared with its bulk state[36]. All shear-exfoliated pnictogens depict enhanced catalytic properties towards the oxidation of ascorbic acid. In particular, antimonene showed dramatic lowering of the oxidation of ascorbic acid by 0.1 V compared with bulk Sb (ref. [36]).

The effect of surface characteristics on the electron transfer properties of h-BN is evident in different current signals of h-BN immobilized on various carbon-based substrates. Using a $[Ru(NH_3)_2]^{3+/2+}$ redox probe, the HET rate declines with increasing h-BN mass deposition, which denotes slower electrode kinetics occurring on h-BN surfaces relative to the underlying carbon-based substrates[57]. When h-BN is modified on smooth substrates, like the glassy carbon electrode, the cathodic current signal shows only minor increases in intensity. However, there is a substantial rise in cathodic current upon the use of h-BN modified on a screen-printed electrode, which presented a rough and ridged surface.

Recently, HET rates of MXenes have also been surveyed. Ti_3C_2, the archetypal MXene, which is terminated with fluorine and oxygen, delayed the electron transfer kinetics of $[Fe(CN)_6]^{3-/4-}$ (ref. [58]). Electrochemical impedance spectroscopic measurement substantiates this with a high R_{ct} value for Ti_3C_2. This is in accordance to the slow electron transfer on a halogen-terminated diamond electrode as a result of the weak interaction between the anionic $[Fe(CN)_6]^{3-/4-}$ and the electronegative fluorine and the hydrophobic surface[59]. Upon alkalization of Ti_3C_2, the electronegative fluorine functional groups were substituted with hydroxyl groups that have lower electronegativity. In doing so, the alk-Ti_3C_2 exhibits faster electron transfer than before and is accompanied by a decline in R_{ct} (ref. [58]).

Industrially important electrocatalysis for clean energy

In a bid to attain affordable and sustainable energy, naturally abundant 2D materials are explored as electrocatalysts in energy-related reactions. These include HER, HOR, ORR and OER: reactions conventionally catalysed by expensive platinum-based materials or precious metal oxides such as IrO_2 or RuO_2. HER is the cathodic reaction in the electrolysis of water whereby the half-reaction is $2H^+ + 2e^- \rightarrow H_2$. In acidic electrolytes, HER occurs in two steps. Commencing with proton adsorption by the Volmer mechanism: $H^+ + e^- + M^* \rightarrow M–H$ (where M^* denotes an adsorption site on the catalyst), the desorption of hydrogen gas then proceeds by the Heyrovsky mechanism: $M–H + H^+ + e^- \rightarrow H_2 + M^*$, or the Tafel mechanism: $2M–H \rightarrow H_2 + M^*$. HOR has the same steps as HER except in reverse. It is important to highlight that while 2D materials such as TMDs are esteemed HER catalysts, their HOR activity tends to be poor. Hitherto most HOR catalysts are limited to metals such as Pt and Rh. Hence, research into developing 2D material catalysts for HOR is encouraged. Complementary to the HER process, OER is the anodic reaction during electrochemical water splitting such that $2H_2O \rightarrow O_2 + 4H^+ + 4e^-$ in acidic electrolytes or $4OH^- \rightarrow 2H_2O + O_2 + 4e^-$ under neutral or alkaline conditions. A single O_2 molecule produced by OER requires four proton and electron transfers in multiple steps and is considered the primary source of inefficiency in most electrolyser systems. ORR is a pertinent reaction in the majority of energy conversion and storage devices; for example, in fuel cells and rechargeable metal–air batteries. ORR proceeds via a direct four-electron pathway or a two-step two-electron process that produces a H_2O_2 intermediate. The carbon dioxide reduction reaction (CO_2RR) is another promising energy conversion process, which reduces CO_2 into a number of useful products including carbon monoxide, formate or methane, amongst others. Due to the assorted products in CO_2RR, many protons, electrons and intermediates are involved.

Mass transfer effects, anisotropy and intrinsic activity of the material dominate the electrocatalytic efficiency of the 2D materials. Mass transfer effects are closely related to the surface structure of material. The anisotropy factor in electrocatalysis is established in the distinct catalytic sites of the 2D material. The intrinsic activity of the material for an electrocatalyst system is evaluated by a volcano-plot relationship, which is a quantitative depiction of the Sabatier's principle. Ideally, an active catalyst binds to the reaction intermediates neither too strongly nor too weakly. Catalyst supports are also employed for catalyst design to optimize the activity. The main 2D catalysts are presented in Table 1.

Mass transport. Favourable mass transport is crucial in highly active catalysts because the rapid depletion of interfacial reactant species (H^+ or OH^-) and generation of gaseous products hinder reaction rates. Thus, continuous reactant supply and rapid gas release are required to maintain the high reaction efficiency. In 2D catalysts, the interstitial spaces between adjacent sheets have been adopted as 2D channels to facilitate mass transport in liquid and gaseous phases[60,61]. Incorporating spacers into MoS_2 nanosheets yielded open, robust and connective channels to achieve accessible surface area and improved ion diffusion, with overall enhanced HER catalyst performance (Fig. 4)[61].

Activity at the edges. The anisotropic factor of 2D materials towards their catalytic properties is demonstrated in the active edges and inert basal planes. Atoms residing on the edges of 2D materials are exposed to a different chemical environment than other parts of the materials with greater propensity for unsaturated coordination compared with basal planes, which are generally of saturated coordination. As the edge sites are responsible for the catalytic activity of the 2D materials, it becomes crucial to optimize the edge structure to enhance their performance. This section highlights prominent studies on edges as active centres of 2D materials in various catalyses.

Graphene edges were experimentally shown to possess higher ORR activity than the basal plane[41]. Graphene edges often contain oxygen groups at the terminals due to oxidation or the starting graphite material. As these oxygen groups may influence the ORR activity, liquid-assisted mechanical exfoliation of graphite was able to acquire graphene with low oxygen content to minimize the effect of oxygen groups on ORR[62]. By this method, nanosized graphene confirmed the abundance of edge sites as the primary reason for enhanced ORR activity. Zigzag edges are the active sites given the propitious thermodynamics. Armchair edges were deemed as inactive due to the strong adsorption of the –OH species that inhibits the active sites for oxygen binding[63]. To eliminate the effect of dopants, an edge-rich and dopant-free graphene demonstrating efficient ORR activity has been developed using Ar plasma-etching[64]. The edge-rich graphene outperformed the pristine graphene with a lower onset potential and higher current density in ORR electrocatalysis. Absence of dopants in the graphene obtained by plasma-etching provides an ideal model to ascertain the role of edges as the ORR active sites on graphene. Similar to graphene, the edges of h-BN are inferred to be the active sites for ORR in a study performed on Au electrodes that concluded with a lower ORR overpotential observed for the h-BN nanosheets than BN nanotubes[65]. BN nanotubes showed few B- and N-edge structures whereas widespread edge structures were noted in BN nanosheets.

In HER electrocatalysis, the edges of TMDs are the catalytic sites as experimentally documented in 2H-MoS_2. By examining a

Table 1 | Summary of key 2D catalysts for catalytic applications

2D catalyst	Synthesis	Application	Performance parameters	Ref.
Graphene, C_3N_4 and BN materials				
Graphene	Ionic liquid-assisted mechanical exfoliation; gradient centrifugation	ORR	Onset potential:−0.13 V vs Ag/AgClCurrent density:−3.85 mA cm^{-2} at −1 V vs Ag/AgCl	62
N-doped graphene nanosheets	Prepared by the reaction of graphene nanosheets with NH_3	ORR	Specific activity at 0.5 V:0.07 to 0.13 electron s^{-1} pyri-N^{-1}	81
Porous BCN nanosheets	Prepared by polymer sol–gel method	ORR	Onset potential: 0.94 V	86
N-doped graphene	High-temperature pyrolysis of graphene oxide and melamine under an N_2 atmosphere	CO_2RR	Onset potential: ~300 mVTafel slope: 135 mV dec^{-1}Maximum Faradaic efficiency of formate production: ~73%	91
N-doped, O-functionalized and edge/defect-rich graphene nanosheets on carbon cloth	Micro-wave plasma enhanced chemical vapour deposition	OER	Overpotential:351 mV at -10 mA cm^{-2}Tafel slope: 38 mV dec^{-1}	92
Co–C_3N_4/carbon nanotube	Polymerization reaction from dicyandiamide and $CoCl_2$•$6H_2O$; annealing; polycondensation reactions	ORR and OER	ORR onset potential: 0.9 VOER onset potential: 1.5 VOER potential of 1.61 V at 10 mA cm^{-2}Tafel slope: 68.4 mV dec^{-1}	94
Transition metal dichalcogenides				
Channelled-engineered MoS_2	Hydrothermal method; intercalation of carbon black particles	HER	Overpotential:360 mV at -100 mA cm^{-2}Tafel slope: 39.4 mV dec^{-1}	61
Double-gyroid MoS_2	Electrodeposition on Si template; sulfidation with H_2S; etching of Si template	HER	Tafel slope: 50 mV dec^{-1}	67
$MoSe_2$ nanofilms on carbon fibre paper	Deposition of Mo films on Si nanowires by magnetron sputtering; selenization	HER	Tafel slope: 59.8 to 63.9 mV dec^{-1}Exchange current density:3.8×10^{-4} to 2.8×10^{-3} mA cm^{-2}	68
1T-MoS_2 nanosheets	Chemical exfoliation by Li intercalation	HER	Overpotential:187 mV at -10 mA cm^{-2}Tafel slope: 43 mV dec^{-1}	71
MoS_2	Commercially obtained	CO_2RR	Overpotential:54 mV at -3.4 mA cm^{-2}Onset potential: -0.164 VReduction current intensity:65 mA cm^{-2} at −0.764 VFaradaic efficiency of CO formation: ~98%	74
WSe_2 nanoflakes	Chemical vapour transport	CO_2RR	Overpotential:54 mV at -18.95 mA cm^{-2}Reduction current intensity:330 mA cm^{-2} at −0.764 VTurnover frequency: 0.28 s^{-1}	75
Layered double hydroxides				
Exfoliated CoCo, NiCo and NiFe LDHs	CoCo and NiCo LDHs were prepared via a topochemical approach; NiFe LDH was obtained by a hydrothermal process; inter-layer anion exchange	OER	Overpotential:300–350 mV at 10 mA cm^{-2}Tafel slope: 40 to 45 mV dec^{-1}	76
Ultrafine NiFe-LDH	Ultrasonication of LDH monolayer precursor in formamide	OER	Overpotential:254 mV at 10 mA cm^{-2}Tafel slope: 32 mV dec^{-1}	77
Exfoliated CoFe-LDH nanosheets	Water-plasma-enabled exfoliation	OER	Overpotential:232 mV at 10 mA cm^{-2}Tafel slope: 36 mV dec^{-1}	95
Black phosphorus				
Few-layer black phosphorus nanosheets	Liquid exfoliation; centrifugation	OER	Onset potential:1.45 V at 0.1 mA cm^{-2}Tafel slope: 88 mV dec^{-1}	78
Te-doped black phosphorus	Chemical vapour transport reaction; in situ surface doping	OER	Onset potential: 1.49 V	93
MXenes				
Mo_2CT_x	HF etching of the parent ternary carbides Mo_2Ga_2C	HER	Overpotential:283 mV at -10 mA cm^{-2}Tafel slope: 70 to 82 mV dec^{-1}	73

All potentials are reported versus reversible hydrogen electrode (RHE) unless otherwise indicated.

monolayer of MoS_2 nanoparticles of various sizes deposited on a Au(111) surface, HER activity showed a linear correlation with the number of edge sites on the MoS_2 catalyst[66]. A prominent example of attaining a high fraction of exposed edge sites is the synthesis of a mesoporous MoS_2 structure with double-gyroid morphology[67]. The curvature of the double-gyroid MoS_2 catalyst exposes a high density of edge sites that resulted in enhanced HER activity. The orientation of the TMDs on the substrate is another consideration whereby MoS_2, $MoSe_2$ and WSe_2 films were aligned vertically on substrates, which maximized their edge-termination, to enhance the catalytic

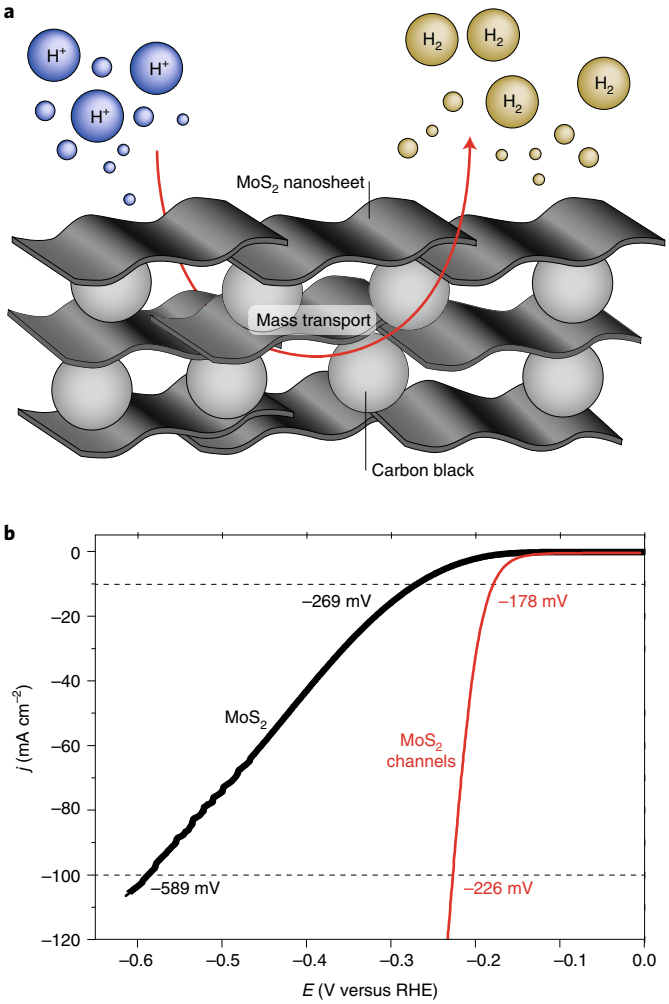

Fig. 4 | Mass transport affects electrocatalytic performance of 2D materials. a, Schematic illustration of engineered channels in MoS_2. **b**, Catalytic HER performance of MoS_2 nanosheets and MoS_2 with engineered channels. Credit: Figure reproduced from ref. [61], American Chemical Society

HER efficiency[68]. However, studies have suggested that the basal planes of the metallic 1T-phase of TMDs, like their edges, are also active towards HER[69,70]. Exfoliated 1T-phase group VIB TMDs nanosheets exhibited superior catalytic HER activity to that of the 2H-phase as exemplified in the low Tafel slope of 1T-MoS_2 of 43 mV dec^{-1} due to an increase in the number of active sites and the higher conductivity of the 1T-phase of TMDs[71,72]. Besides TMDs as HER electrocatalysts, MXenes equipped with O* or OH* termination are also promising candidates though pristine MXenes are rarely used as catalysts given their low activity. It is interesting to highlight that the O* basal planes of most MXenes are active for HER. In particular, delamination of Mo_2CT_x improved HER activity despite having a higher fraction of exposed basal planes[73].

Surprisingly, edges of TMDs are also active for CO_2RR in the presence of ionic liquids as co-catalysts despite being the active sites for HER, a competing reaction to CO_2RR in acidic conditions. CO_2 reduction to CO occurs at the Mo-terminated edges of MoS_2 due to their metallic character and high *d*-electron density[74]. The ionic liquid, 1-ethyl-3-methylimidazolium tetrafluoroborate (EMIM-BF_4), stabilizes CO_2 via complex formation and deters HER. A series of TMD nanoflakes including WS_2 and WSe_2 possessing higher density of edges than their bulk counterparts exhibit enhanced CO_2RR catalysis[75]. This is most accentuated for WSe_2 nanoflakes terminated with W atoms.

Among 2D materials, layered metal oxides and LDHs are most frequently exploited as OER catalysts attributed to their outstanding OER efficiency where edges account for their OER activity. A liquid-phase exfoliation of bulk LDHs (NiFe, NiCo, CoCo) into monolayers resulted in up to 4.5 times higher OER catalysis than before, comparable to IrO_2 catalysts (Fig. 5)[76]. Moreover, OER activity is further improved upon fracturing single-layered NiFe LDHs into ultrafine nanosheets of <3 nm thickness with maximally exposed edges[77]. When black phosphorus is thinned into nanosheets by liquid exfoliation followed by centrifugation, additional OER-active sites are generated. These generated sites are proposed to be the edges[78]. Compared with bulk phosphorus, the nanosheets exhibit improved OER performance with an onset at 1.45 V and Tafel slope of 88 mV dec^{-1} (ref. [78]).

Introducing impurities and defects. Although 2D materials showcase innate activity towards electrocatalysis originating from their active sites, in their pristine states electrocatalysis is limited by the number of active sites and is only mild. Therefore, introducing impurities such as dopants or even additional functional groups can maximize the intrinsic activity of 2D materials for catalyses. As edges are the catalytically active sites of the 2D materials, doping or attaching functional groups at the edges could amplify changes to their catalytic performance. Doping or functionalization at basal sites could tweak the intrinsic activity of inert basal planes. Defect engineering is an established method to enhance the intrinsic activity of active sites. Surface structural defects encompass edges with low coordination numbers; hence the dangling bonds, and the presence of atom vacancies.

Among 2D materials, the doping of graphene and h-BN materials is a conventional strategy to optimize their ORR catalytic properties. Graphene sheets doped with heteroatoms have demonstrated high electrocatalytic activity for ORR. Heteroatom doping modulates the chemical reactivity and electronic properties of graphene. Amongst all heteroatom-doped graphene, N-doped graphene is most extensively investigated. Dai and co-workers reported N-doped graphene, which was prepared by chemical vapour deposition, as an efficient metal-free ORR electrocatalyst that undergoes a direct four-electron pathway in alkaline conditions[79]. The origin of ORR catalytic activity is traced to graphitic and pyridinic N moieties. Graphitic N transfers the electron density to the graphene lattice, strengthening the nucleophilicity of adjacent carbon atoms and, in turn, facilitates oxygen adsorption[80]. Pyridinic N functions as an ORR active site[81]. Substitution of multiple heteroatoms in graphene to yield dual-doped graphene elicits synergistic effects. For example, co-doping of B and N in graphene resulted in ORR activity that was almost Pt-like, superior to that of its singly doped B or N counterparts[82]. Within a B–C–N hetero-ring in graphene, N is an electron-withdrawing group that activates B to become the active site. This synergy decreases with increasing distance between B and pyridinic-N atoms. Presence of metal dopants also enhances the electrocatalytic performance of graphene. Traces of Mn (0.0018 wt%) are responsible for ORR activity in metal-free graphene[83]. Carbon-doping of h-BN nanosheets manifests high spin and charge density that lowers the energy gap, therefore promoting oxygen adsorption and facilitating an ORR pathway requiring a lower barrier than a Pt-based catalyst[84]. Decorating Au nanoparticles on the surface of h-BN nanosheets reduced the ORR overpotential by 0.5 V compared with before due to the stabilization of an adsorbed O atom by the Au_8 cluster that supported the four-electron pathway[85]. Incorporating the merits of graphene and h-BN, porous BCN nanosheets are created using a polymer sol–gel method[86]. Apart from the high concentration of pyridinic N, which accelerates oxygen adsorption, the B–N–C groups at the edges enable OH adsorption and O protonation processes. Hence, porous BCN nanosheets exhibit commendable catalytic ORR behaviour in both alkaline and acidic conditions, rivalling that of Pt/C.

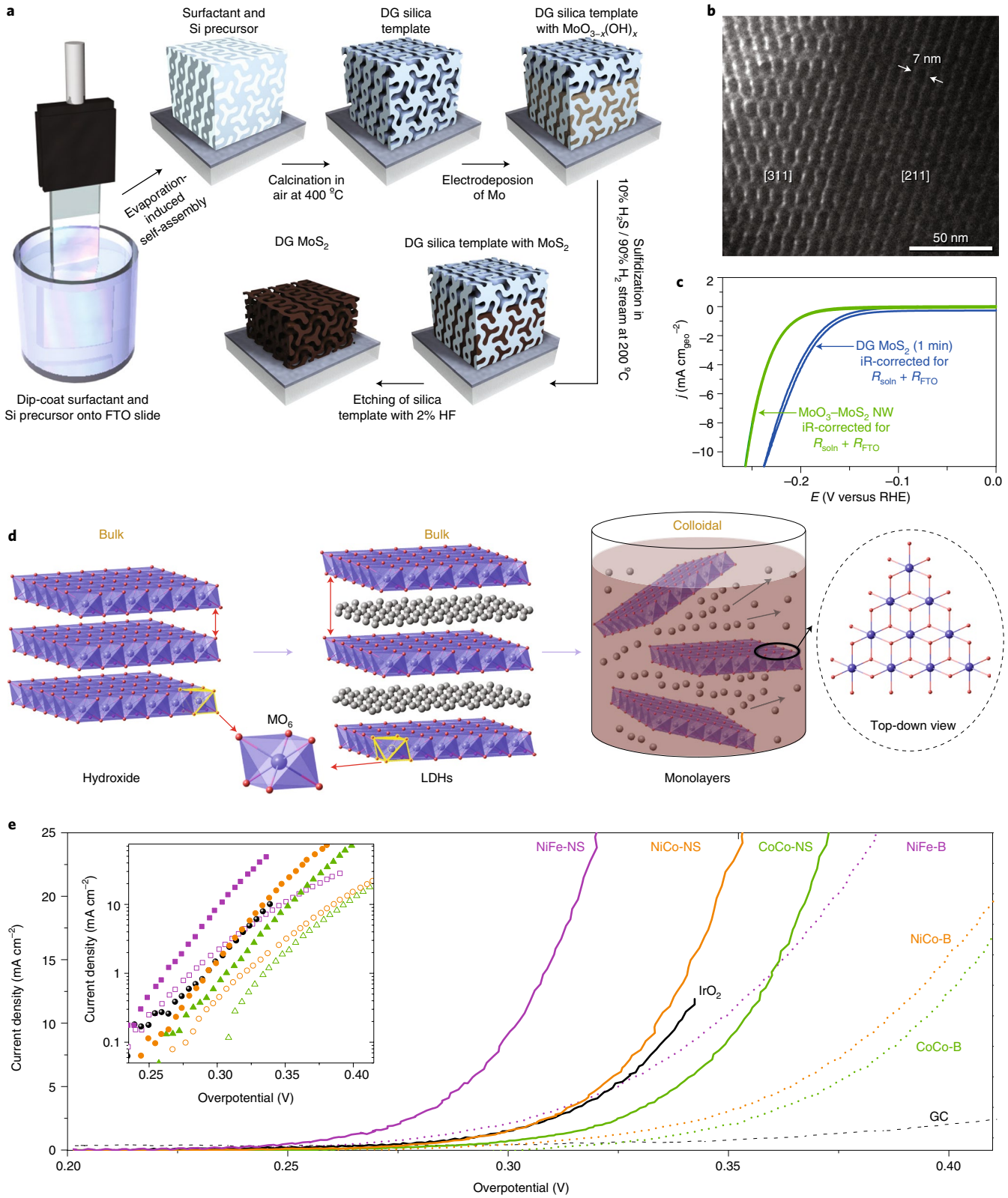

Fig. 5 | Maximizing active sites for electrocatalysis of energy-related reactions. a, Synthesis of double gyroid (DG) mesoporous MoS_2. **b**, Transmission electron micrograph of double gyroid mesoporous MoS_2. **c**, Comparison between the catalytic HER performance of double-gyroid MoS_2 and MoO_3-MoS_2 nanowires (iR-corrected for resistances from the flourine-doped tin oxide substrate and the solution). **d**, Exfoliation of bulk LDHs to nanosheets. **e**, Comparisons of catalytic OER performance of bulk and exfoliated LDHs. Credit: Figure reproduced from ref. [67], SNL (**a**–**c**) and ref. [76], SNL (**d**,**e**)

Incorporating metals or non-metallic atoms also effectively improves the intrinsic HER catalytic activity of TMDs. It is established that a key criterion to estimate the intrinsic activity for HER is correlated to the Gibbs free energy of adsorbed H (ΔG_H) where a near-zero value is ideal for a HER catalyst. After doping the S edge of MoS_2 and WS_2 with Co, ΔG_H of the S edge in both TMDs became more favourable for HER as confirmed theoretically and experimentally[24]. The inert S edges and basal planes of 2H-MoS_2 were also activated by P-doping, evident in the reduction of Mo valence charge and the lowering of ΔG_H for the nearby S atoms of P towards zero[87]. Therefore, P-doped 2H-MoS_2 exhibited onset potential (130 mV) and low Tafel slope (49 mV dec^{-1}); both are attributes of superior HER electrocatalytic activity compared with the undoped 2H-MoS_2.

Although the basal plane of graphene has a large positive ΔG_H, which inhibits HER, doping graphene with heteroatoms results in modified electronic properties that improve HER. Qiao and co-workers evaluated various single and dual heteroatom-doped graphene by combining both experimental and DFT calculations[88]. The lowering of ΔG_H on the basal planes of B-, N-, S- and P-doped graphene to over a range of 0.6 to 1 eV was computed for the C atom adjacent to the dopant element which is deemed as the HER-active site on graphene. These singly doped graphene materials showed a Tafel slope ~120 mV dec^{-1} corresponding to the adsorption step being rate-determining. Dual doping could enhance their intrinsic HER activity further, whereby N,S-doped graphene and N,P-doped graphene showcase lower overpotential than that of the singly-doped control sample. It is also important to acknowledge that the HER performance of these doped graphene materials paled in comparison to MoS_2.

Introducing functional groups on the basal plane may alter the HER activity of MXenes[73,89]. By experimental and theoretical methods, a recent study examined the effect of functionalization (T_x) on the HER of Ti- and Mo-based MXenes[89]. Higher fluorine coverage on the basal plane of $Ti_3C_2T_x$ demonstrated lower HER activity. Similarly, Mo_2CT_x at low fluorine coverage on the basal plane was found to be an active and stable HER catalyst with an overpotential of 189 mV at −10 mA cm^{-2}.

Heteroatom-doped graphene catalysts have also been frequently explored for CO_2RR. B- and N-doped graphene, respectively, demonstrate efficient formate and CO production[90,91]. The asymmetric charge and spin density in B-graphene led to active B and C atoms for chemisorption, whereas the pyridinic N is identified as the active adsorption site for intermediate COOH* to form CO. Thus, the type of dopant could present a potential point of control to effect selective CO_2RR for desired products.

Doped 2D materials are also predominant in OER catalysis. Chief amongst graphene-based OER catalysts, a recent work designed N-doped, O-functionalized and edge-rich graphene nanosheets on a carbon cloth[92]. The combination of numerous functional groups and active sites on the surface of the graphene nanosheets led to an outstanding OER activity. This catalyst design outperformed undoped graphene with an overpotential of 351 mV and Tafel slope of 38 mV dec^{-1}, surpassing that of the state-of-the-art OER catalysts like RuO_2. Being a relatively new addition to the class of 2D materials, doping of black phosphorus has also been explored to improve the capability as an OER catalyst. Te-doped black phosphorus nanosheets that were acquired by chemical vapour transport followed by subsequent liquid exfoliation, manifested lower OER onset potential than the undoped nanosheets[93]. Interestingly, g-C_3N_4 when incorporated with transition metals show bifunctional properties as ORR and OER catalysts as demonstrated in a series of metal-C_3N_4 complexes[94]. One example is Co-C_3N_4 wherein the Co-N_2 moiety occurs in the C_3N_4 matrix. The altered *d*-band position led to favourable adsorption energy of ORR and OER intermediates.

Although the creation of structural defects is known to improve activity of 2D materials for various electrocatalytic reactions, this strategy has been most popularly utilized on LDHs to modify electronic structure and hence, achieve higher OER performance (Fig. 6). Defects in the form of oxygen and metal vacancies tailor the electronic properties of the surface due to their electron and orbital distribution. Metal vacancies elevate the valency of metal centres in proximity and improve OER activity. Exfoliation of CoFe-LDHs via plasma techniques resulted in multiple vacancies of Co, Fe and O (refs [95,96]). These vacancies are postulated to lower the adsorption energy of water and facilitate OER. The water-plasma exfoliated CoFe-LDH nanosheets exhibited outstanding OER catalytic activity with an overpotential of 232 mV and Tafel slope of 36 mV dec^{-1}.

Catalyst support. Mounting 2D catalysts on supports with high specific surface area is an efficient strategy to develop enhanced catalyst performance. Carbon supports are attractive and widely utilized due to a suitable dispersion platform that promotes efficient electron transfer. Compared to NiFe-LDH or NiFe-LDH mixed with carbon nanotubes, solvothermal synthesis of ultrathin NiFe-LDH grown on oxidized carbon nanotubes showcased higher OER activity[97]. Strong interactions between NiFe-LDH and carbon nanotubes strengthened electron transfer kinetics for OER. Heteroatom doping and addition of functional groups to carbon supports are also effective at facilitating interactions between catalyst and support. A 3D catalyst with NiCo-LDH grown on N-doped graphene hydrogels outperformed that grown on the undoped graphene[98]. The enhanced HER performance of MoS_2 nanoparticles prepared on reduced graphene oxides (RGO) relative to the absence of RGO highlighted that the use of RGO provided a well nanoparticle dispersion that increased the accessibility of edge sites and better electron transport[99].

Conclusion and future outlook

The rich electrochemistry of 2D materials provides opportunities to discover their applications in energy catalysis. Despite the diversity of 2D materials, their resultant electrocatalytic and charge transfer properties are attributed to anisotropy and surface characteristics. We shed light on the inherent electrochemistry arising from intrinsic elemental make-up, surface oxides or oxygen groups. Across most 2D materials, edges display faster electron transfer and higher electrocatalytic activity against the sluggish electron transfer of basal planes. The role of surface impurities or additional functional groups may also modify electron transfer properties.

2D materials have garnered much success in ORR, HER, OER and CO_2RR electrocatalysis where the edges are the catalytic active centres. Nanostructuring materials to attain optimal morphology or exfoliation of materials into thinner and smaller nanoflakes are often implemented to increase density of active edge sites. Using catalyst supports further improves the accessibility of these active sites. Integration of dopants and functional groups also enhances intrinsic catalytic activity. Broadly, graphene is a forthcoming choice as an ORR catalyst, TMDs takes the helm as an intrinsic HER electrocatalyst while LDHs and associated oxides are best for catalysing OER. Burgeoning research into MXenes also showed potential as HER catalysts. The use of 2D materials as CO_2RR has room for expansion as works to date mainly report TMDs and graphene-based materials. The challenge in CO_2RR also lies in fabricating catalysts with high product selectivity. Employing 2D materials such as h-BN, g-C_3N_4 and the pnictogens as energy-related electrocatalysts is limited and further investigations would elucidate their catalytic potential. Beyond TMDs and graphene, MXenes are the next promising electrocatalysts and are predicted to outperform the TMDs because the basal planes of MXenes upon functionalization may become catalytic and function as additional active sites. Published works for h-BN, g-C_3N_4 and the pnictogens as electrocatalysts are

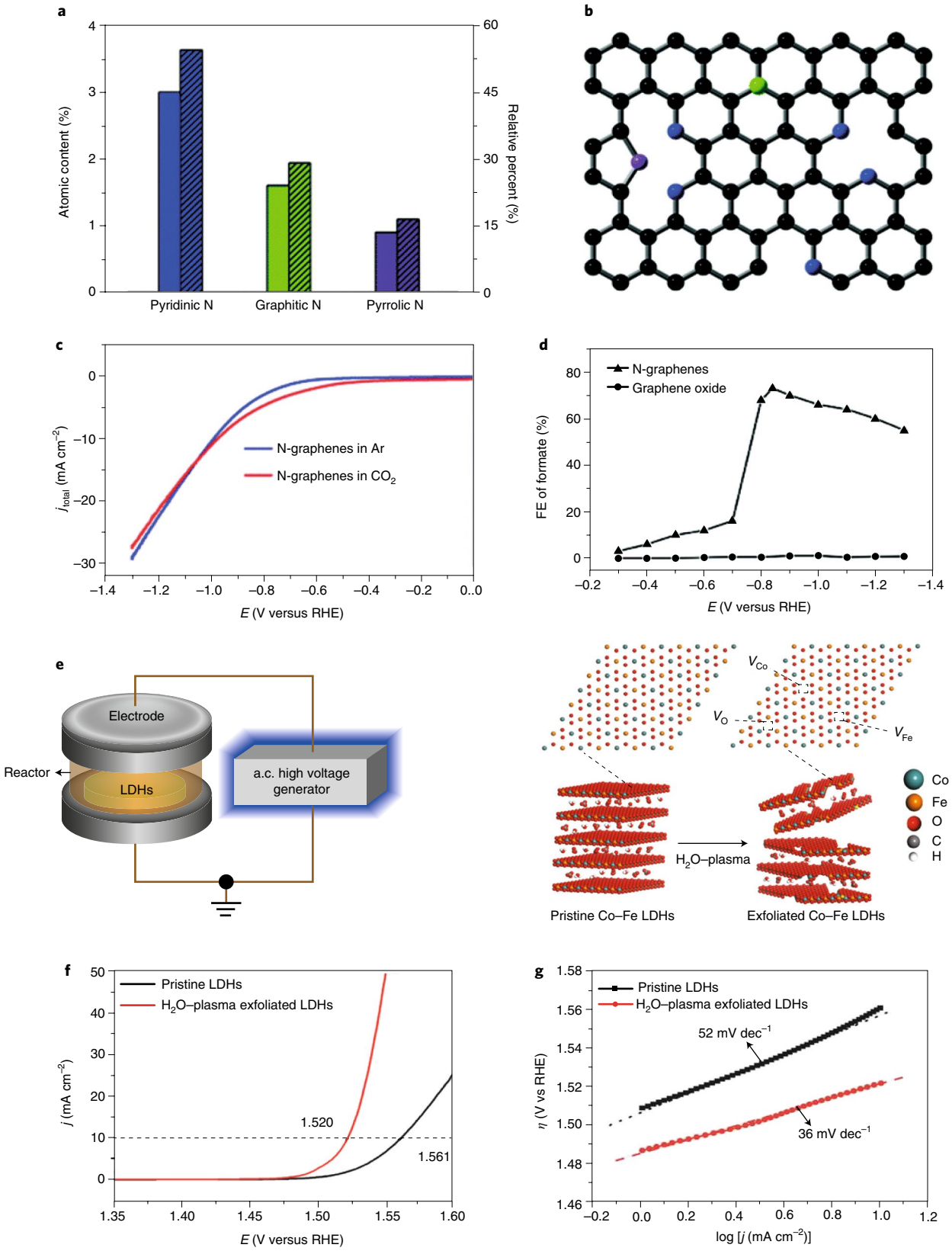

Fig. 6 | Increasing the intrinsic activity for enhanced electrocatalysis in energy-related reactions. a, Statistical N atomic content and relative percentage in N-graphene. **b**, Various N configurations in N-graphene. **c**, Linear sweep voltammograms of N-graphene catalyst in Ar- and CO_2-saturated $KHCO_3$. **d**, Comparison between Faradaic efficiency (FE) of N-graphene and graphene oxide across applied potentials. **e**, Scheme depicting water–plasma-enabled exfoliation of CoFe LDH nanosheets with multiple vacancies generated. **f**,**g**, Linear sweep voltammograms (**f**) and Tafel plots (**g**) showcasing OER performance between pristine LDHs and water–plasma exfoliated LDHs. Credit: figure reproduced from ref. [91], Wiley (**a**–**d**) and ref. [95], Wiley (**e**–**g**)

currently few, though efforts have been undertaken either by doping or developing hybrids with better catalytic attributes.

Moving forward, the field of 2D nanomaterials is brimming with possibilities. The development of hybrid 2D materials by integrating two or more materials could create novel composite structures that display unique functionality and tailored properties for specific applications. Anisotropy and surface characteristics could serve as guidelines when designing different compounds.

Received: 13 May 2018; Accepted: 18 October 2018;
Published online: 3 December 2018

References

1. Geim, A. K. & Novoselov, K. S. The rise of graphene. *Nat. Mater.* **6**, 183–191 (2007).
2. Zhang, H. Ultrathin two-dimensional nanomaterials. *ACS Nano* **9**, 9451–9469 (2015).
3. Xu, M., Liang, T., Shi, M. & Chen, H. Graphene-like two-dimensional materials. *Chem. Rev.* **113**, 3766–3798 (2013).
4. Chia, X., Eng, A. Y. S., Ambrosi, A., Tan, S. M. & Pumera, M. Electrochemistry of nanostructured layered transition-metal dichalcogenides. *Chem. Rev.* **115**, 11941–11966 (2015).
5. Chhowalla, M. et al. The chemistry of two-dimensional layered transition metal dichalcogenide nanosheets. *Nat. Chem.* **5**, 263–275 (2013).
6. Carvalho, A. et al. Phosphorene: from theory to applications. *Nat. Rev. Mater.* **1**, 16061 (2016).
7. Pumera, M. & Sofer, Z. 2D monoelemental arsenene, antimonene, and bismuthene: beyond black phosphorus. *Adv. Mater.* **29**, 1605299 (2017).
8. Jin, H. et al. Emerging two-dimensional nanomaterials for electrocatalysis. *Chem. Rev.* **118**, 6337–6408 (2018).
9. Wang, Y., Wang, X. & Antonietti, M. Polymeric graphitic carbon nitride as a heterogeneous organocatalyst: from photochemistry to multipurpose catalysis to sustainable chemistry. *Angew. Chem. Int. Ed.* **51**, 68–89 (2012).
10. Ambrosi, A., Chua, C. K., Bonanni, A. & Pumera, M. Electrochemistry of graphene and related materials. *Chem. Rev.* **114**, 7150–7188 (2014).
11. Py, M. A. & Haering, R. R. Structural destabilization induced by lithium intercalation in MoS_2 and related compounds. *Can. J. Phys.* **61**, 76–84 (1983).
12. Wilson, J. A. & Yoffe, A. D. The transition metal dichalcogenides discussion and interpretation of the observed optical, electrical and structural properties. *Adv. Phys.* **18**, 193–335 (1969).
13. Chia, X., Sutrisnoh, N. A. A., Sofer, Z., Luxa, J. & Pumera, M. Morphological effects and stabilization of the metallic 1T phase in layered V-, Nb-, and Ta-Doped WSe_2 for electrocatalysis. *Chem. Eur. J.* **24**, 3199–3208 (2018).
14. Enyashin, A. N. et al. New route for stabilization of 1T-WS_2 and MoS_2 phases. *J. Phys. Chem. C* **115**, 24586–24591 (2011).
15. Tang, Q. & Jiang, D.-E. Stabilization and band-gap tuning of the 1T-MoS_2 monolayer by covalent functionalization. *Chem. Mater.* **27**, 3743–3748 (2015).
16. Cavani, F., Trifirò, F. & Vaccari, A. Hydrotalcite-type anionic clays: preparation, properties and applications. *Catal. Today* **11**, 173–301 (1991).
17. Miller, T. S. et al. Carbon nitrides: synthesis and characterization of a new class of functional materials. *Phys. Chem. Chem. Phys.* **19**, 15613–15638 (2017).
18. Naguib, M. et al. Two-dimensional nanocrystals produced by exfoliation of Ti_3AlC_2. *Adv. Mater.* **23**, 4248–4253 (2011).
19. Anasori, B., Lukatskaya, M. R. & Gogotsi, Y. 2D metal carbides and nitrides (MXenes) for energy storage. *Nat. Rev. Mater.* **2**, 16098 (2017).
20. Zhang, Q. et al. MoS_2 yolk–shell microspheres with a hierarchical porous structure for efficient hydrogen evolution. *Nano Res.* **9**, 3038–3047 (2016).
21. Mashtalir, O. et al. Intercalation and delamination of layered carbides and carbonitrides. *Nat. Commun.* **4**, 1716 (2013).
22. Chua, C. K., Sofer, Z. & Pumera, M. Graphite oxides: effects of permanganate and chlorate oxidants on the oxygen composition. *Chem. Eur. J.* **18**, 13453–13459 (2012).
23. Zhou, M. et al. Controlled synthesis of large-area and patterned electrochemically reduced graphene oxide films. *Chem. Eur. J.* **15**, 6116–6120 (2009).
24. Bonde, J., Moses, P. G., Jaramillo, T. F., Norskov, J. K. & Chorkendorff, I. Hydrogen evolution on nano-particulate transition metal sulfides. *Faraday Discuss.* **140**, 219–231 (2009).
25. Chia, X., Ambrosi, A., Sofer, Z., Luxa, J. & Pumera, M. Catalytic and charge transfer properties of transition metal dichalcogenides arising from electrochemical pretreatment. *ACS Nano* **9**, 5164–5179 (2015).
Illustrates the electrotreatment method of tuning the heterogeneous electron transfer properties of the layered transition metal dichalcogenides whereby a reductive treatment accelerates the electron transfer rate while an oxidation hinders the electron transfer.
26. Eng, A. Y. S., Ambrosi, A., Sofer, Z., Šimek, P. & Pumera, M. Electrochemistry of transition metal dichalcogenides: strong dependence on the metal-to-chalcogen composition and exfoliation method. *ACS Nano* **8**, 12185–12198 (2014).
27. Tan, S. M., Sofer, Z., Luxa, J. & Pumera, M. Aromatic-exfoliated transition metal dichalcogenides: implications for inherent electrochemistry and hydrogen evolution. *ACS Catal.* **6**, 4594–46071 (2016).
28. Luxa, J. et al. Layered transition-metal ditellurides in electrocatalytic applications—contrasting properties. *ACS Catal.* **7**, 5706–5716 (2017).
29. Jaegermann, W. & Schmeisser, D. Reactivity of layer type transition metal chalcogenides towards oxidation. *Surf. Sci.* **165**, 143–160 (1986).
30. Kautek, W. & Gerischer, H. Anisotropic photocorrosion of n-type MoS_2, $MoSe_2$, and WSe_2 single crystal surfaces: the role of cleavage steps, line and screw dislocations. *Surf. Sci.* **119**, 46–60 (1982).
31. Gholamvand, Z. et al. Comparison of liquid exfoliated transition metal dichalcogenides reveals $MoSe_2$ to be the most effective hydrogen evolution catalyst. *Nanoscale* **8**, 5737–5749 (2016).
32. Chia, X. et al. Layered platinum dichalcogenides (PtS_2, $PtSe_2$, and $PtTe_2$) electrocatalysis: monotonic dependence on the chalcogen size. *Adv. Funct. Mater.* **26**, 4306–4318 (2016).
33. Chia, X., Ambrosi, A., Lazar, P., Sofer, Z. & Pumera, M. Electrocatalysis of layered group 5 metallic transition metal dichalcogenides (MX_2, M = V, Nb, and Ta; X = S, Se, and Te). *J. Mater. Chem. A* **4**, 14241–14253 (2016).
34. Wang, L., Sofer, Z. & Pumera, M. Voltammetry of layered black phosphorus: electrochemistry of multilayer phosphorene. *ChemElectroChem* **2**, 324–327 (2015).
35. Favron, A. et al. Photooxidation and quantum confinement effects in exfoliated black phosphorus. *Nat. Mater.* **14**, 826–832 (2015).
36. Gusmão, R., Sofer, Z., Bouša, D. & Pumera, M. Pnictogen (As, Sb, Bi) nanosheets for electrochemical applications are produced by shear exfoliation using kitchen blenders. *Angew. Chem. Int. Ed.* **56**, 14417–14422 (2017).
37. Fu, Y., Zhu, J., Hu, C., Wu, X. & Wang, X. Covalently coupled hybrid of graphitic carbon nitride with reduced graphene oxide as a superior performance lithium-ion battery anode. *Nanoscale* **6**, 12555–12564 (2014).
38. Yew, Y. T. et al. Electrochemistry of layered graphitic carbon nitride synthesised from various precursors: searching for catalytic effects. *ChemPhysChem* **17**, 481–488 (2016).
39. Lorencova, L. et al. Electrochemical performance of $Ti_3C_2T_x$ MXene in aqueous media: towards ultrasensitive H_2O_2 sensing. *Electrochim. Acta* **235**, 471–479 (2017).
40. Davies, T. J., Hyde, M. E. & Compton, R. G. Nanotrench arrays reveal insight into graphite electrochemistry. *Angew. Chem. Int. Ed.* **44**, 5121–5126 (2005).
41. Yuan, W. et al. The edge- and basal-plane-specific electrochemistry of a single-layer graphene sheet. *Sci. Rep.* **3**, 2248 (2013).
42. McCreery, R. L. Advanced carbon electrode materials for molecular electrochemistry. *Chem. Rev.* **108**, 2646–2687 (2008).
43. Tan, C. et al. Reactivity of monolayer chemical vapor deposited graphene imperfections studied using scanning electrochemical microscopy. *ACS Nano* **6**, 3070–3079 (2012).
44. Chua, C. K., Ambrosi, A. & Pumera, M. Graphene oxide reduction by standard industrial reducing agent: thiourea dioxide. *J. Mater. Chem.* **22**, 11054–11061 (2012).
45. Ji, X., Banks, C. E., Crossley, A. & Compton, R. G. Oxygenated edge plane sites slow the electron transfer of the ferro-/ferricyanide redox couple at graphite electrodes. *ChemPhysChem* **7**, 1337–1344 (2006).
46. Ahmed, S. M. & Gerischer, H. Influence of crystal surface orientation on redox reactions at semiconducting MoS_2. *Electrochim. Acta* **24**, 705–711 (1979).
47. Tan, S. M. et al. Pristine basal- and edge-plane-oriented molybdenite mos_2 exhibiting highly anisotropic properties. *Chem. Eur. J.* **21**, 7170–7178 (2015).
48. Wu, S. et al. Electrochemically reduced single-layer mos_2 nanosheets: characterization, properties, and sensing applications. *Small* **8**, 2264–2270 (2012).
49. Chia, X., Ambrosi, A., Sedmidubský, D., Sofer, Z. & Pumera, M. Precise tuning of the charge transfer kinetics and catalytic properties of mos_2 materials via electrochemical methods. *Chem. Eur. J.* **20**, 17426–17432 (2014).
50. Chia, X., Sofer, Z., Luxa, J. & Pumera, M. Layered noble metal dichalcogenides: tailoring electrochemical and catalytic properties. *ACS Appl. Mater. Interfaces* **9**, 25587–25599 (2017).
51. Poh, H. L., Simek, P., Sofer, Z., Tomandl, I. & Pumera, M. Boron and nitrogen doping of graphene via thermal exfoliation of graphite oxide in a BF_3 or NH_3 atmosphere: contrasting properties. *J. Mater. Chem. A* **1**, 13146–13153 (2013).
52. Wang, Y., Shao, Y., Matson, D. W., Li, J. & Lin, Y. Nitrogen-doped graphene and its application in electrochemical biosensing. *ACS Nano* **4**, 1790–1798 (2010).
53. Wong, C. H. A., Chua, C. K., Khezri, B., Webster, R. D. & Pumera, M. Graphene oxide nanoribbons from the oxidative opening of carbon nanotubes retain electrochemically active metallic impurities. *Angew. Chem. Int. Ed.* **52**, 8685–8688 (2013).

54. Chee, S. Y. & Pumera, M. Metal-based impurities in graphenes: application for electroanalysis. *Analyst* **137**, 2039–2041 (2012).
55. Chua, X. J. et al. negative electrocatalytic effects of p-doping niobium and tantalum on MoS_2 and WS_2 for the hydrogen evolution reaction and oxygen reduction reaction. *ACS Catal.* **6**, 5724–5734 (2016).
56. Sofer, Z. et al. Layered black phosphorus: strongly anisotropic magnetic, electronic, and electron-transfer properties. *Angew. Chem. Int. Ed.* **55**, 3382–3386 (2016).
57. Khan, A. F. et al. 2D hexagonal boron nitride (2D-hBN) explored as a potential electrocatalyst for the oxygen reduction reaction. *Electroanalysis* **29**, 622–634 (2017).
58. Zhu, X. et al. Alkaline intercalation of Ti_3C_2 MXene for simultaneous electrochemical detection of Cd(II), Pb(II), Cu(II) and Hg(II). *Electrochim. Acta* **248**, 46–57 (2017).
59. Kondo, T. et al. Plasma etching treatment for surface modification of boron-doped diamond electrodes. *Electrochim. Acta* **52**, 3841–3848 (2007).
60. Menzel, N., Ortel, E., Kraehnert, R. & Strasser, P. Electrocatalysis using porous nanostructured materials. *ChemPhysChem* **13**, 1385–1394 (2012).
61. Wang, G. et al. Engineering two-dimensional mass-transport channels of the MoS_2 nanocatalyst toward improved hydrogen evolution performance. *ACS Appl. Mater. Interfaces* **10**, 25409–25414 (2018).
Highlights the significance of mass transport channels in layered materials towards enhancing their electrocatalytic hydrogen evolution efficiency.
62. Benson, J. et al. Tuning the catalytic activity of graphene nanosheets for oxygen reduction reaction via size and thickness reduction. *ACS Appl. Mater. Interfaces* **6**, 19726–19736 (2014).
Demonstrates the abundant graphene edges as the dominant factor in the activity of graphene catalyst towards oxygen reduction reaction.
63. Deng, D. et al. Size effect of graphene on electrocatalytic activation of oxygen. *Chem. Commun.* **47**, 10016–10018 (2011).
64. Tao, L. et al. Edge-rich and dopant-free graphene as a highly efficient metal-free electrocatalyst for the oxygen reduction reaction. *Chem. Commun.* **52**, 2764–2767 (2016).
65. Uosaki, K. et al. Boron nitride nanosheet on gold as an electrocatalyst for oxygen reduction reaction: theoretical suggestion and experimental proof. *J. Am. Chem. Soc.* **136**, 6542–6545 (2014).
66. Jaramillo, T. F. et al. Identification of active edge sites for electrochemical h_2 evolution from MoS_2 nanocatalysts. *Science* **317**, 100–102 (2007).
67. Kibsgaard, J., Chen, Z., Reinecke, B. N. & Jaramillo, T. F. Engineering the surface structure of MoS_2 to preferentially expose active edge sites for electrocatalysis. *Nat. Mater.* **11**, 963–969 (2012).
Highlights that morphological engineering of MoS_2 materials to expose edge sites improves electrocatalytic hydrogen evolution reaction.
68. Wang, H. et al. $MoSe_2$ and WSe_2 nanofilms with vertically aligned molecular layers on curved and rough surfaces. *Nano Lett.* **13**, 3426–3433 (2013).
69. Tsai, C., Chan, K., Nørskov, J. K. & Abild-Pedersen, F. Theoretical insights into the hydrogen evolution activity of layered transition metal dichalcogenides. *Surf. Sci.* **640**, 133–140 (2015).
70. Voiry, D. et al. Conducting MoS_2 nanosheets as catalysts for hydrogen evolution reaction. *Nano Lett.* **13**, 6222–6227 (2013).
71. Lukowski, M. A. et al. Enhanced hydrogen evolution catalysis from chemically exfoliated metallic MoS_2 nanosheets. *J. Am. Chem. Soc.* **135**, 10274–10277 (2013).
72. Lukowski, M. A. et al. Highly active hydrogen evolution catalysis from metallic WS_2 nanosheets. *Energy Environ. Sci.* **7**, 2608–2613 (2014).
73. Seh, Z. W. et al. Two-dimensional molybdenum carbide (MXene) as an efficient electrocatalyst for hydrogen evolution. *ACS Energy Lett.* **1**, 589–594 (2016).
Demonstrates that the basal planes of MXenes are also active sites for hydrogen evolution reaction.
74. Asadi, M. et al. Robust carbon dioxide reduction on molybdenum disulphide edges. *Nat. Commun.* **5**, 4470 (2014).
75. Asadi, M. et al. Nanostructured transition metal dichalcogenide electrocatalysts for CO_2 reduction in ionic liquid. *Science* **353**, 467–470 (2016).
Elucidates exfoliation of layered transition metal dichalcogenides to nanosheets which exhibit enhanced CO_2 reduction efficiency compared to their bulk counterparts due to the generation of a higher number of edges.
76. Song, F. & Hu, X. Exfoliation of layered double hydroxides for enhanced oxygen evolution catalysis. *Nat. Commun.* **5**, 4477 (2014).
Shows liquid-phase exfoliated layered double hydroxides that possess accessible active sites and enhanced electron transport which increases their catalytic oxygen evolution efficiency.
77. Zhao, Y. et al. Sub-3 nm ultrafine monolayer layered double hydroxide nanosheets for electrochemical water oxidation. *Adv. Energy Mater.* **8**, 1703585 (2018).
78. Ren, X. et al. Few-layer black phosphorus nanosheets as electrocatalysts for highly efficient oxygen evolution reaction. *Adv. Energy Mater.* **7**, 1700396 (2017).
79. Qu, L., Liu, Y., Baek, J.-B. & Dai, L. Nitrogen-doped graphene as efficient metal-free electrocatalyst for oxygen reduction in fuel cells. *ACS Nano* **4**, 1321–1326 (2010).
80. Luo, Z. et al. Pyridinic N doped graphene: synthesis, electronic structure, and electrocatalytic property. *J. Mater. Chem.* **21**, 8038–8044 (2011).
81. Guo, D. et al. Active sites of nitrogen-doped carbon materials for oxygen reduction reaction clarified using model catalysts. *Science* **351**, 361–365 (2016).
82. Zheng, Y., Jiao, Y., Ge, L., Jaroniec, M. & Qiao, S. Z. Two-step boron and nitrogen doping in graphene for enhanced synergistic catalysis. *Angew. Chem. Int. Ed.* **52**, 3110–3116 (2013).
83. Wang, L., Ambrosi, A. & Pumera, M. "Metal-free" catalytic oxygen reduction reaction on heteroatom-doped graphene is caused by trace metal impurities. *Angew. Chem. Int. Ed.* **52**, 13818–13821 (2013).
Demonstrates that traces of metal impurities are sufficient to influence the performance of graphene as an oxygen reduction reaction catalyst.
84. Zhao, J. & Chen, Z. Carbon-doped boron nitride nanosheet: an efficient metal-free electrocatalyst for the oxygen reduction reaction. *J. Phys. Chem. C* **119**, 26348–26354 (2015).
85. Elumalai, G., Noguchi, H., Lyalin, A., Taketsugu, T. & Uosaki, K. Gold nanoparticle decoration of insulating boron nitride nanosheet on inert gold electrode toward an efficient electrocatalyst for the reduction of oxygen to water. *Electrochem. Commun.* **66**, 53–57 (2016).
86. Wang, J. et al. Porous boron carbon nitride nanosheets as efficient metal-free catalysts for the oxygen reduction reaction in both alkaline and acidic solutions. *ACS Energy Lett.* **2**, 306–312 (2017).
87. Huang, X. et al. Activating basal planes and S-terminated edges of MoS_2 toward more efficient hydrogen evolution. *Adv. Funct. Mater.* **27**, 1604943 (2017).
Depicts that functionalization of the inert basal planes and S-edges of MoS_2 by doping resulted in enhanced catalyst behaviour for hydrogen evolution reaction.
88. Jiao, Y., Zheng, Y., Davey, K. & Qiao, S.-Z. Activity origin and catalyst design principles for electrocatalytic hydrogen evolution on heteroatom-doped graphene. *Nat. Energy* **1**, 16130 (2016).
89. Handoko, A. D. et al. Tuning the basal plane functionalization of two-dimensional metal carbides (MXenes) to control hydrogen evolution activity. *ACS Appl. Energy Mater.* **1**, 173–180 (2018).
90. Sreekanth, N., Nazrulla, M. A., Vineesh, T. V., Sailaja, K. & Phani, K. L. Metal-free boron-doped graphene for selective electroreduction of carbon dioxide to formic acid/formate. *Chem. Commun.* **51**, 16061–16064 (2015).
91. Wang, H., Chen, Y., Hou, X., Ma, C. & Tan, T. Nitrogen-doped graphenes as efficient electrocatalysts for the selective reduction of carbon dioxide to formate in aqueous solution. *Green Chem.* **18**, 3250–3256 (2016).
92. Li, D., Ren, B., Jin, Q., Cui, H. & Wang, C. Nitrogen-doped, oxygen-functionalized, edge- and defect-rich vertically aligned graphene for highly enhanced oxygen evolution reaction. *J. Mater. Chem. A* **6**, 2176–2183 (2018).
93. Zhang, Z., Khurram, M., Sun, Z. & Yan, Q. Uniform tellurium doping in black phosphorus single crystals by chemical vapor transport. *Inorg. Chem.* **57**, 4098–4103 (2018).
94. Zheng, Y. et al. Molecule-level g-C_3N_4 coordinated transition metals as a new class of electrocatalysts for oxygen electrode reactions. *J. Am. Chem. Soc.* **139**, 3336–3339 (2017).
95. Liu, R., Wang, Y., Liu, D., Zou, Y. & Wang, S. Water-plasma-enabled exfoliation of ultrathin layered double hydroxide nanosheets with multivacancies for water oxidation. *Adv. Mater.* **29**, 1701546 (2017).
Elucidates water–plasma-enabled exfoliation of layered CoFe double hydroxide nanosheets that generates multiple Co, Fe and O vacancies, which lower the adsorption energy of water, in turn leading to an enhanced catalytic oxygen evolution reaction.
96. Wang, Y. et al. Layered double hydroxide nanosheets with multiple vacancies obtained by dry exfoliation as highly efficient oxygen evolution electrocatalysts. *Angew. Chem.* **129**, 5961–5965 (2017).
97. Gong, M. et al. An advanced Ni–Fe layered double hydroxide electrocatalyst for water oxidation. *J. Am. Chem. Soc.* **135**, 8452–8455 (2013).
98. Chen, S., Duan, J., Jaroniec, M. & Qiao, S. Z. Three-dimensional n-doped graphene hydrogel/NiCo double hydroxide electrocatalysts for highly efficient oxygen evolution. *Angew. Chem. Int. Ed.* **52**, 13567–13570 (2013).
99. Li, Y. et al. MoS_2 nanoparticles grown on graphene: an advanced catalyst for the hydrogen evolution reaction. *J. Am. Chem. Soc.* **133**, 7296–7299 (2011).

Acknowledgements

X.C. acknowledges financial support from the Nanyang President Graduate Scholarship. This work was supported by the project Advanced Functional Nanobots (reg. No. CZ.02.1.01/0.0/0.0/15_003/0000444 financed by the EFRR).

Competing interests

The authors declare no competing interests.

Additional information

Reprints and permissions information is available at www.nature.com/reprints.

Correspondence should be addressed to M.P.

Publisher's note: Springer Nature remains neutral with regard to jurisdictional claims in published maps and institutional affiliations.